Corrosion Science 94 (2015) 142–155

Contents lists available at ScienceDirect

Corrosion Science

journal homepage: www.elsevier.com/locate/corsci

Improvement of corrosion resistance and biocompatibility of rare-earth WE43 magnesium alloy by neodymium self-ion implantation

Weihong Jin [a], Guosong Wu [a], Hongqing Feng [a], Wenhao Wang [a,b], Xuming Zhang [a], Paul K. Chu [a,*]

[a] Department of Physics and Materials Science, City University of Hong Kong, Tat Chee Avenue, Kowloon, Hong Kong, China
[b] Department of Orthopaedics & Traumatology, The University of Hong Kong, Pokfulam Road, Hong Kong, China

ARTICLE INFO

Article history:
Received 28 November 2014
Accepted 29 January 2015
Available online 4 February 2015

Keywords:
A. Magnesium
B. Ion implantation
B. EIS
B. Polarization
B. SEM

ABSTRACT

Without introducing extraneous elements, a small amount of Nd is introduced into rare-earth WE43 magnesium alloy by ion implantation. The surface composition, morphology, polarization, and electrochemical properties, as well as weight loss, pH, and leached ion concentrations after immersion, are systematically evaluated to determine the corrosion behavior. The cell adhesion and viability are also determined to evaluate the biological response *in vitro*. A relatively smooth and hydrophobic surface layer composed of mainly Nd_2O_3 and MgO is produced and degradation of WE43 is significantly retarded. Furthermore, significantly enhanced cell adhesion and excellent biocompatibility are observed after Nd self-ion implantation.

1. Introduction

Biodegradable metals have attracted much attention due to their potential application to temporary implants, including cardiovascular stents [1–3] and orthopedic implants [4,5]. Magnesium-based and iron-based alloys are the primary biodegradable metals, which are capable of degrading relatively safely within the body [6,7], and in particular, magnesium alloys are very promising in biomedical applications [6,8]. Rare-earth magnesium alloys have the advantage that they do not contain aluminum, which may be detrimental to neurons [9]. For example, WE43 Mg alloy, which contains yttrium (Y) and neodymium (Nd), is one of the attractive biomedical rare-earth magnesium alloys [10,11]. Y serves as an effective solid solution hardener because the difference in the atomic radii between Mg and Y atoms is quite large and Y may be introduced in a considerable quantity due to its high solubility in magnesium [12]. As a rare-earth element with limited solubility, Nd contributes to the enhancement of the anticorrosive properties [13]. Therefore, addition of small quantities of Y and Nd can modify the microstructure and improve the mechanical properties and corrosion resistance of magnesium alloys. Compared to other traditional biomedical materials, such as stainless steels, titanium alloys, and cobalt–chromium alloys, magnesium alloys degrade spontaneously in the physiological environment and a follow-up surgery is not needed to remove the implants after healing [14]. Moreover, the elastic modulus of magnesium alloys matches that of bone, thereby avoiding the stress-shielding effect, which can reduce new bone growth [8]. Additionally, magnesium is an essential element in the human body, plays a vital role in metabolic processes [15], and benefits bone growth [16,17]. However, the rapid degradation rate of magnesium alloys in the aggressive physiological environment has so far limited wider clinical adoption because of mechanical integrity loss before sufficient healing [8], as well as excessive hydrogen evolution during degradation [18]. Unlike products for the automotive, aerospace, and electronics industry, biomedical magnesium implants require both good biocompatibility, as well as controlled degradation. In fact, the ideal biodegradable candidate should have a suitable degradation rate to allow the implant to maintain mechanical support during tissue healing while being nontoxic and compatible to cells [19,20].

Surface treatment is commonly performed to improve the corrosion resistance and biocompatibility of magnesium-based biomedical implants [19–22]. Unlike conventional techniques such as coatings, ion implantation does not change the geometric dimensions of the specimens and introduces a graded surface layer without an abrupt interface, thereby minimizing the risk of layer delamination. Consequently, ion implantation is one of the most effective ways to improve the surface properties of Mg alloys [16,23–25]. Neodymium in the RE WE43 magnesium alloy improves the mechanical properties mainly by grain boundary strengthening, due to the formation of the intermetallic phase in the grain boundary [13,14,26]. It has also been reported that Nd

* Corresponding author. Tel.: +852 34427724; fax: +852 34420542.
E-mail address: paul.chu@cityu.edu.hk (P.K. Chu).

http://dx.doi.org/10.1016/j.corsci.2015.01.049
0010-938X/

can enhance the corrosion resistance of magnesium alloys due to suppression of the galvanic effects by the intermetallic compounds [13,15,27,28] and the surface layer containing neodymium oxide [7,15,22,29]. In addition, Nd has been shown to be biocompatible as relatively high concentrations can be tolerated by various cell types [17,25,30]. In this work, without introducing extraneous elements, a small amount of Nd is ion implanted into WE43 Mg alloy and the effects on the corrosion resistance and biocompatibility as well as mechanisms are studied systematically.

2. Experimental details

2.1. Ion implantation and surface characterization

The as-cast WE43 (Mg–3.79 wt.%Y–2.43 wt.%Nd–1.55wt% Gd–0.52 wt.%Zr) magnesium alloy was cut into 10 mm × 10 mm × 2 mm plates, ground using different successive grades of SiC abrasive paper (up to 1200 grit), ultrasonically cleaned in ethanol for 10 min, and dried in air. Nd ion implantation was conducted on a metal ion implanter equipped with a neodymium cathodic arc source (HEMII-80, Plasma Technology Ltd., Hong Kong SAR) for 5 h at an accelerating voltage of 30 kV and a base pressure of 5.0×10^{-4} Pa in the vacuum chamber.

The elemental depth profiles and chemical states were determined by X-ray photoelectron spectroscopy (XPS, PHI 5802, Physical Electronics, Inc., USA) with Al Kα irradiation. The sputtering rate was estimated to be about 7.8 nm/min based on a SiO_2 reference. The surface morphology before and after ion implantation was examined by scanning electron microscopy (SEM, JSM-820, JEOL Ltd., Japan) and atomic force microscopy (AFM, Auto Probe CP, Park Scientific Instruments, USA). The contact angle measurements were performed using 4 μl water droplets on a contact angle goniometer (Model 200, Ramé-Hart, USA) at room temperature and the average value was calculated from three measurements conducted on three different samples. The hardness and elastic modulus were determined by a nano-indenter (Nano Indenter XP, MTS Systems Corporation, USA).

2.2. Corrosion studies

Electrochemical measurements were conducted on an electrochemical workstation (Zennium, Zahner, Germany) using a three-electrode cell. A saturated calomel electrode (SCE) served as the reference electrode, a platinum rod was used as the counter electrode, and the sample constituted the working electrode. All the potentials were relative to SCE if not specified. The electrochemical experiments were conducted in both simulated body fluids (SBF) and complete cell culture medium (cDMEM) composed of Dulbecco's Modified Eagle Medium (DMEM, Gibco, Life Technologies, USA) and 10% fetal bovine serum (FBS, Gibco, Life Technologies, USA) at 37 °C. The SBF solution with a pH of 7.40 contained ions with the following concentrations: 142.0 Na^+, 5.0 K^+, 1.5 Mg^{2+}, 2.5 Ca^{2+}, 147.8 Cl^-, 4.2 HCO_3^-, 1.0 HPO_4^-, and 0.5 SO_4^- mM, which are close to those in human blood plasma. The SBF was prepared by dissolving the following reagent grade chemicals: 8.035 g/L NaCl, 0.355 g/L $NaHCO_3$, 0.225 g/L KCl, 0.231 g/L $K_2HPO_4{\cdot}3H_2O$, 0.311 g/L $MgCl_2{\cdot}6H_2O$, 1.0 M HCl (39 mL), 0.292 g/L CaCl2, and 0.072 g/L Na2SO4 in distilled water and then buffered at pH 7.4 using 6.118 g/l trishydroxymethyl aminomethane and 1.0 M HCl [31]. The area exposed to the solution was 1 cm^2 during the electrochemical measurements. After immersion in the solution for 5 min, electrochemical impedance spectroscopy (EIS) was performed in the frequency between 100 kHz and 100 mHz with a 10 mV peak-to-peak alternating signal at the open circuit potential (OCP). The polarization curves were then acquired at a scanning rate of 1 mV s^{-1} from −300 mV and 500 mV with respect to the OCP. To monitor the degradation of the untreated and Nd-implanted magnesium alloys, immersion tests were carried out in SBF. The specimens were immersed in 20 mL of SBF and maintained at 37 °C. At each time point, 3 samples were studied to obtain an average value for weight loss, pH, and ion concentrations. At different immersion time of 1, 3, and 7 days, the specimens were taken out from the SBF and the corrosion products formed on the sample surface were removed using chromic acid (200 g L^{-1} CrO_3 + 10 g L^{-1} $AgNO_3$). The samples were then rinsed with deionized water and dried overnight for subsequent weight measurements. The pH of the extracted SBF was monitored at the three intervals. The concentrations of leached magnesium, alloying elements, calcium, and phosphate species were determined by inductively-coupled plasma optical emission spectroscopy (ICP-OES, PE Optima 2100DV, Perkin Elmer, USA). In addition, both the surface morphology and composition of the untreated and Nd-implanted WE43 samples after immersion in SBF for 2, 12, and 36 h were examined by SEM equipped with energy dispersive X-ray spectroscopy (EDS, INCAx-sight, Oxford Instruments, UK).

2.3. In vitro studies

Mouse MC3T3-E1 pre-osteoblasts were used in the *in vitro* cell culture experiments. The MC3T3-E1 cells were cultured in DMEM supplemented with 10% FBS at 37 °C in a humidified atmosphere with 5% CO_2. Prior to the cell adhesion experiments, the samples were sterilized with 70 vol% ethanol for 30 min and rinsed three times with sterile phosphate-buffered saline (PBS). The MC3T3-E1 cells were seeded on the untreated and Nd-implanted WE43 samples on a 24-well culture plate at a density of 5×10^4 cells per well. After incubation for 5 h, the seeded samples were rinsed three times with sterile PBS and fixed with 4% paraformaldehyde for 15 min. The cytoskeleton protein F-actin was stained with fluorescein phalloidin (Invitrogen, Life Technologies, USA) and the nuclei were stained with 4′,6-diamidino-2-phenylindole (DAPI, Beyotime Institute of Biotechnology, China). Finally, the cell images were captured by a fluorescence microscope (Axio Observer Z1, Carl Zeiss, Germany).

The *in vitro* cell viability was evaluated by an indirect method. The untreated and Nd-implanted WE43 samples were first immersed into DMEM at 37 °C in a humidified atmosphere with 5% CO_2 for 3 days. The ratio of the sample surface area to DMEM was 1.25 cm^2/mL. The solution was collected and filtered through a 0.22 μm filter (Merck Millipore, Germany) for the following experiments. The extracts were stored at 4 °C and supplemented with 10% FBS prior to usage. 5.0×10^3 MC3T3-E1 cells per well were seeded on a 96-well culture plate. After incubation for 24 h, the medium was replaced by 100 μl of the medium containing different concentrations of the extracts. The control groups were treated with DMEM supplemented with 10% FBS. After incubation for 1 and 3 days, 10 μL of (3-(4,5-dimethylthiazol-2-yl)-2,5-diphenyltetrazolium bromide were added to each well and after incubating for another 4 h, 100 μL dimethyl sulfoxide was added to dissolve the formed formazen. The absorbance was determined at 570 nm on a microplate spectrophotometer (BioTek Eon, BioTek Instruments Inc., USA). The cell viability is calculated by (OD_{sample}/$OD_{control}$) * 100%.

3. Results and discussion

3.1. Surface characterization

The XPS depth profile of the Nd-implanted WE43 is depicted in Fig. 1 and the high-resolution Mg 1s, Y 3d, Nd 3d, and O 1s spectra

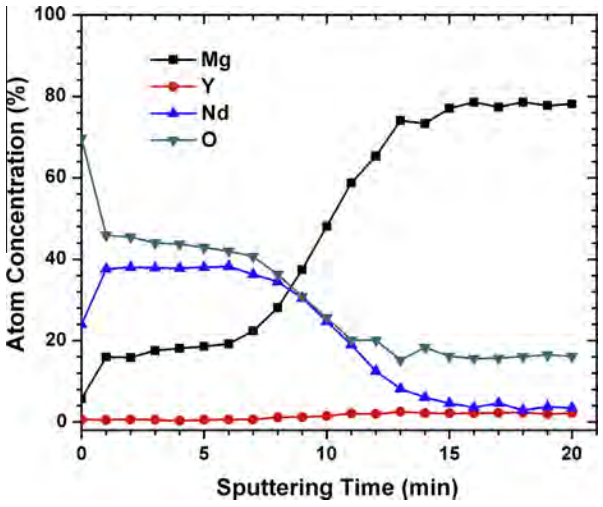

Fig. 1. XPS depth profile of the Nd-implanted WE43.

of the Nd-implanted WE43 are shown in Fig. 2. As shown in Fig. 1, a thin Nd-rich layer is formed on the Nd-implanted WE43 sample and the peak Nd concentration is about 38%. Compared to the bulk substrate with a size of 10 mm × 10 mm × 2 mm, the amount of Nd implanted is much smaller since the implanted depth of Nd is approximately 160 nm. Oxygen is also observed from the top layer as well as relatively deeply into the Nd-implanted sample possibly due to the formation of magnesium oxide/hydroxide [32] and oxygen contamination [33]. The high-resolution Nd 3d spectrum in Fig. 2(c) shows Nd $3d^{5/2}$ at 982.6 eV, which indicates the formation of Nd_2O_3 on the surface of the implanted sample [34]. The valence state of neodymium gradually changes to the metallic state accompanied by gradually declining O 1s intensity (Fig. 2(d)) with increasing sputtering time. The Nd_2O_3 layer is about 70 nm, which acts as the main barrier against corrosion of the magnesium substrate in the corrosive environment. The surface magnesium exists in the form of oxidized state (Mg^{2+}), which may be assigned to magnesium oxide/hydroxide [32]. As shown in Fig. 2(a), the magnesium peak intensity from 0 to 6 min is very weak, indicating small amounts of magnesium oxide/hydroxide in the top layer. As sputtering continues, some of the magnesium changes into the metallic state (Mg^0), while oxidized magnesium is still detected, indicating the formation MgO [16,23] in a relatively thick layer, which can further serve as a barrier against magnesium corrosion. Yttrium is not abundant in the near surface as inferred from the decreased yttrium signal after Nd implantation but after sputtering for 9 min, yttrium is detected in the metallic state [33,35]. As shown in Fig. 2(d), the oxygen peak at 0 min corresponds to the formation of Nd_2O_3 and $Mg(OH)_2$/MgO compounds. With increasing sputtering time, the oxygen peaks shift toward the negative direction and then the positive direction, suggesting that the content of Nd_2O_3 increases and then decreases. The trend is in accordance with the results in Fig. 2(c). After sputtering for 12 min, the oxygen peak is attributed to the formation of MgO. This suggests that Nd ion implantation produces Nd_2O_3 in the top layer

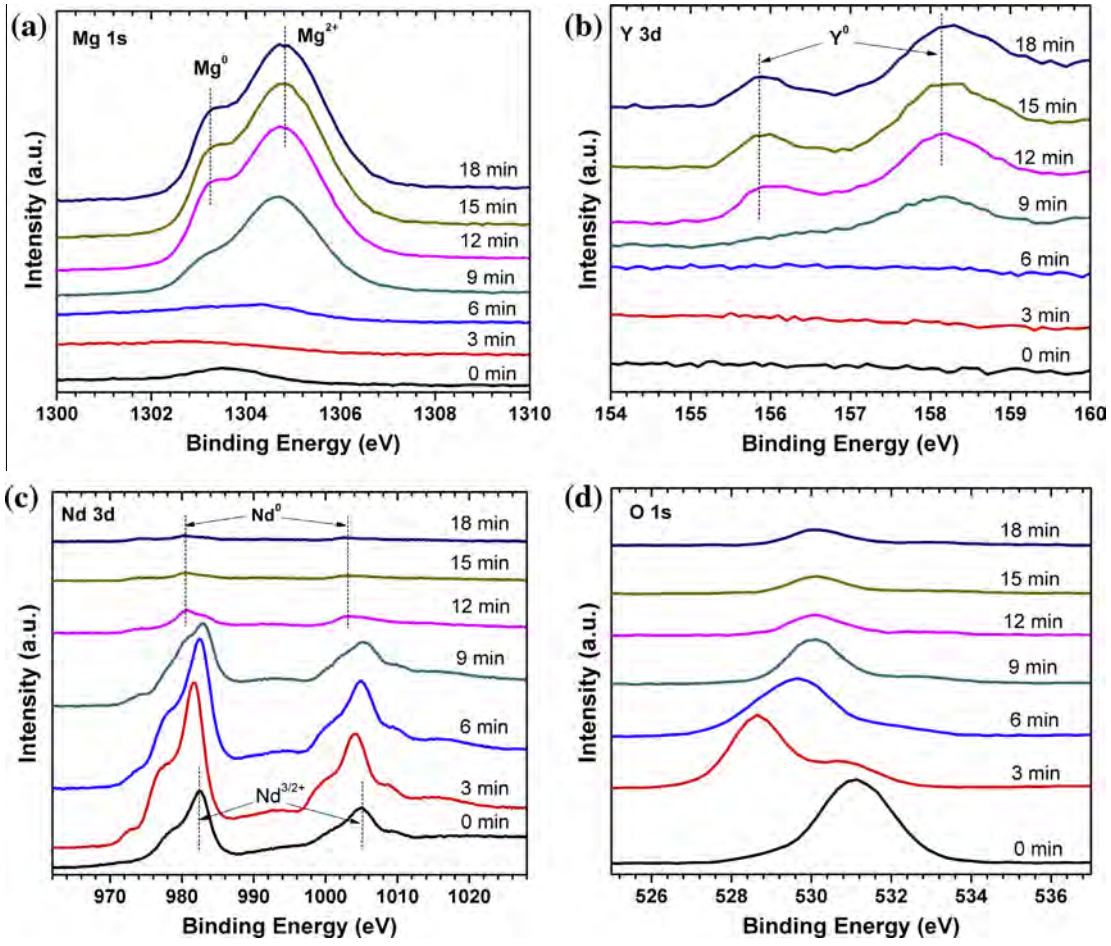

Fig. 2. High-resolution XPS spectra of (a) Mg 1s, (b) Y 3d, (c) Nd 3d, and (d) O 1s acquired at different sputtering time from the Nd-implanted WE43.

and MgO in the inner layer, both of which keep the Mg substrate away from the external aggressive medium to lessen corrosion.

The SEM and AFM images of the WE43 samples before and after Nd ion implantation are depicted in Fig. 3, which reveals obvious changes in the surface morphology after ion implantation. The untreated sample has a relatively rough surface with some scratches produced by mechanical grinding (Fig. 3a and c), but the surface becomes smoother after Nd ion implantation, with only some intrusions appearing on the surface of the Nd-implanted sample surface (Fig. 3b and d). The α-Mg matrix and some second phases with different size and shape (referring to the arrows) are also present in the microstructure of the WE43 sample before and after ion implantation. The root-mean-square roughness value of the untreated WE43 is 10.9 nm, which is larger than 1.2 nm of the Nd-implanted WE43 (scanned area of 5 μm × 5 μm). Generally, the surface roughness of the materials affects the corrosion resistance. A smooth surface is beneficial to corrosion resistance due to the relatively homogeneous structure and small difference in the electrode potential between the peaks and valleys [36–38]. Since Nd ion implantation results in a relatively smooth surface, the corrosion resistance is expected to improve. Fig. 4 shows the water contact angles measured from the untreated and Nd-implanted WE43 samples. The contact angle of the untreated WE43 sample is 35.8°, while that of the Nd-implanted sample increases to 71.2°. A larger contact angle is related to lower surface energy indicating that the Nd-implanted surface is more hydrophobic. Fig. 5 shows the hardness and elastic modulus values of the untreated and Nd-implanted WE43 samples. The mechanical performance is an important consideration for biomedical magnesium alloys [39]. Compared to traditional biomedical materials, magnesium alloys have relatively low strength, which needs to be enhanced to providing firm support. Generally, the materials hardness is proportional to the materials strength [40] and a bigger Young modulus is related to larger plastic resistance [41]. There have been research activities trying to improve the surface mechanical properties of different biomedical materials using different methods [42,43]. With increasing displacement into the surface, the hardness and elastic modulus decrease gradually due to the gradient structure and then reach stable values representing the values of the bulk substrate. The results show that Nd ion implantation improves the surface mechanical properties.

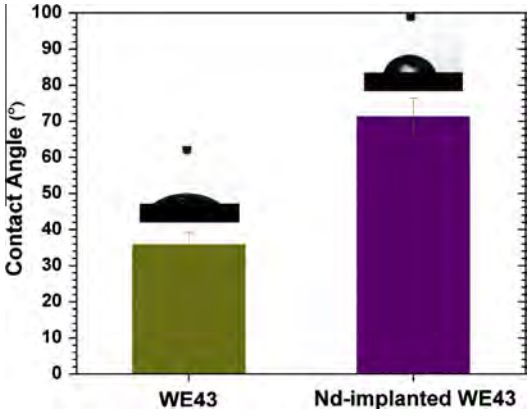

Fig. 4. Water contact angles on the untreated and Nd-implanted WE43.

3.2. Corrosion behavior

Before the EIS and polarization tests, the OCP of the untreated and Nd-implanted WE43 were observed for 300 s after immersion in SBF and cDMEM at 37 °C as shown in Fig. 6. In both SBF and cDMEM, the OCP of the untreated and Nd-implanted WE43 exhibits noble shifts with respect to the immersion time. At the beginning, the potential of the untreated WE43 is −2030 mV and −1794 mV in SBF and DMEM, respectively, while the potential of the Nd-implanted WE43 is −1920 mV and −1761 mV in SBF and DMEM, respectively. After immersion for 300 s, compared to the untreated WE43 (about 18 mV vs. SCE in SBF and 59 mV vs. SCE in cDMEM), the Nd-implanted WE43 shows potential shifts of about 67 mV vs. SCE and 78 mV vs. SCE in SBF and cDMEM, respectively. Therefore, the Nd-implanted WE43 shows larger noble potential shifts, which indicates the corrosion rate is likely to be

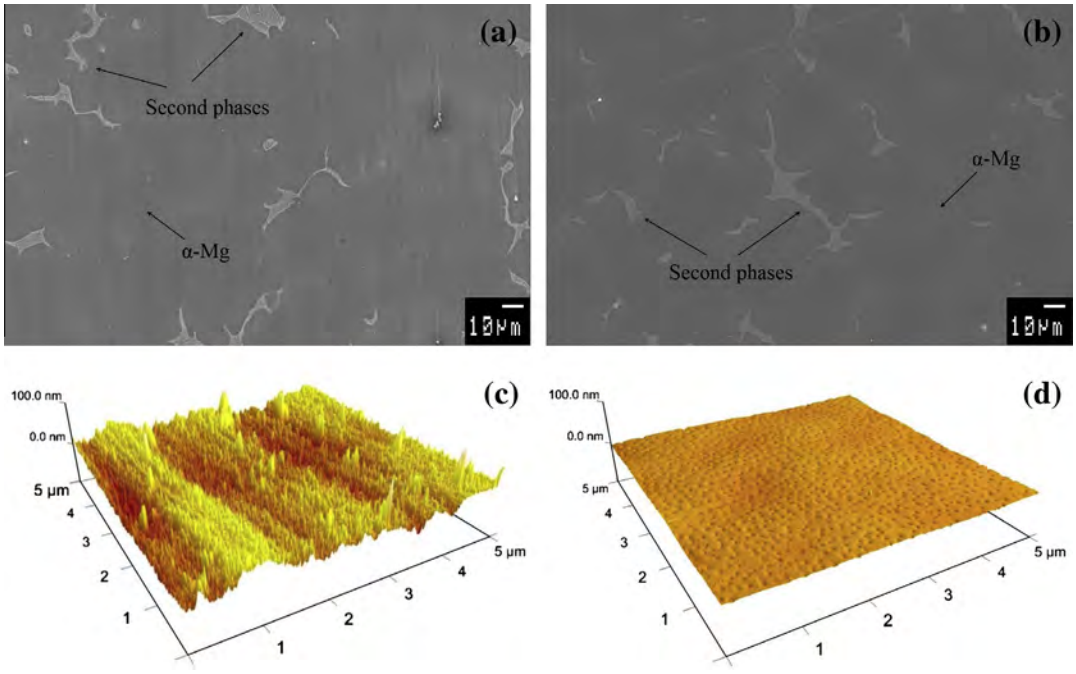

Fig. 3. SEM and AFM images: (a, c) Untreated and (b, d) Nd-implanted WE43.

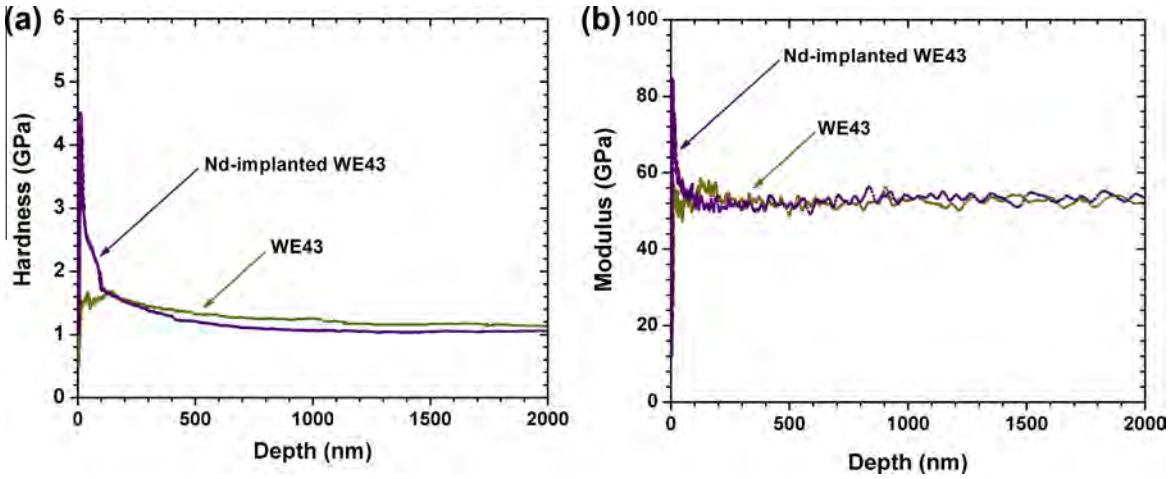

Fig. 5. (a) Hardness and (b) elastic modulus values of the untreated and Nd-implanted WE43.

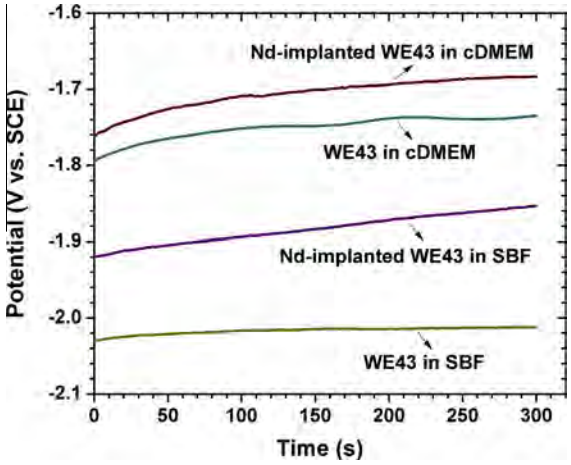

Fig. 6. OCP of the untreated and Nd-implanted WE43 after immersion in SBF and cDMEM for 300 s.

retarded with respect to time and better protection is performed on the Nd-implanted WE43 samples.

Fig. 7(a) and (b) display the polarization curves of the untreated and Nd-implanted WE43 in SBF and cell culture medium. The cathodic and anodic polarization curves represent cathodic hydrogen evolution and anodic dissolution of the samples, respectively. As shown in Fig. 7(a) and (b), the corrosion potential (E_{corr}) and corrosion current density (I_{corr}) are calculated by Tafel extrapolation of the cathodic polarization curve due to a non-symmetrical polarization curve between the anodic and cathodic branches [44,45]. The E_{corr}, I_{corr}, and Tafel slople β_c values obtained from the polarization curves are listed in Table 1. Compared to the untreated WE43 samples (555.7 ± 65.0 μA cm^{-2} in SBF and 2.55 ± 0.79 μA cm^{-2} in the cell culture medium), the Nd-implanted WE43 samples exhibit significantly low I_{corr} of 11.9 ± 4.9 μA cm^{-2} in SBF and 0.50 ± 0.06 μA cm^{-2} in the cell culture medium. The corrosion rate is determined by the corrosion current density, one of the most important parameters in corrosion resistance characterization. The smaller corrosion current density corresponds to a lower corrosion rate. Therefore, corrosion of the WE43 magnesium alloy is significantly retarded by Nd implantation. The corrosion rate of both the untreated and Nd-implanted WE43 is faster in SBF than the cell culture medium, and it is mainly due to the high concentration of chloride ions in SBF [31] and protein adsorption on the materials surface acting as an inhibitor against corrosion in the cell culture medium [46]. The improvement in the corrosion resistance in SBF is more obvious than that in the cell culture medium because I_{corr} shows a 50-fold decrease in SBF but only a 5-fold decrease in the cell culture medium. All in all, the polarization results reveal that Nd implantation deters magnesium degradation both in SBF and cell culture medium.

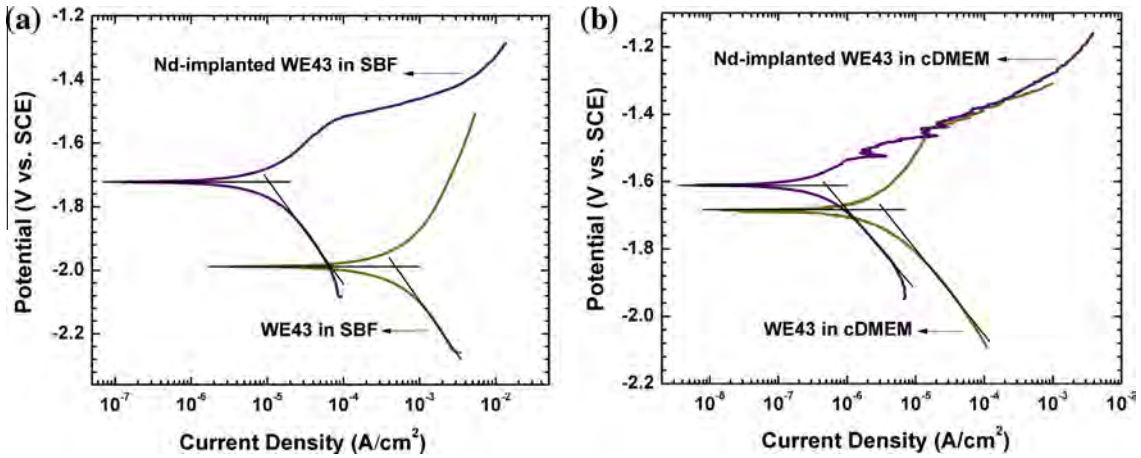

Fig. 7. Polarization curves of the untreated and Nd-implanted WE43 in (a) SBF and (b) cDMEM.

Table 1
E_{corr}, I_{corr}, and β_c values of WE43 and Nd-implanted WE43 in SBF and cDMEM calculated from the polarization curves.

	SBF		cDMEM	
	WE43	Nd-implanted WE43	WE43	Nd-implanted WE43
E_{corr} (mV vs. SCE)	−1992 ± 4	−1740 ± 26	−1705 ± 30	−1560 ± 50
I_{corr} (μA/cm^2)	555.7 ± 65.0	11.9 ± 4.9	2.55 ± 0.79	0.50 ± 0.06
β_c (mV/decade)	−361 ± 21	−335 ± 35	−244 ± 5	−254 ± 65

To investigate and understand the corrosion processes at the electrode/electrolyte interface, EIS is conducted. Fig. 8 depicts the Nyquist plots of the WE43 samples in SBF and cell culture medium before and after ion implantation. Two capacitive loops in the high and low frequency regions are observed from both solutions. They are obvious in SBF and overlap in the cell culture medium. The high frequency capacitive loop is attributed to charge transfer whereas the capacitive loop in the low frequencies results from mass transportation through the corrosion product layer. The Nd-implanted WE43 shows large capacitive loops in both solutions. It is well known that a larger capacitive loop contributes to better corrosion resistance. Therefore, the Nyquist results suggest that the corrosion resistance of the WE43 magnesium alloy is greatly enhanced in SBF and cell culture medium after Nd ion implantation. In the electrical equivalent circuit, each resistor–capacitor parallel circuit corresponds to the relevant capacitive time constant. According to the physical structure of the electrode, two electrical equivalent circuits with two time constants shown in Fig. 8(c) and (d) are used to fit the experimental data of the Nyquist plots for both SBF and cell culture medium, respectively. The same materials may have different EIS behavior in different solutions and different electrical equivalent circuits are used to fit the EIS results [47]. In this work, the EIS plots of the same sample in the two different solutions exhibit two semicircles, but the two semicircles in the cell culture medium are indistinct. SBF is composed of mainly inorganic salts, whereas the cell culture medium also contains some proteins. This may result in different corrosion behavior revealed by different EIS plots. Two relatively clear semicircles appear in the case of SBF, while the two capacitive loops interact with each other for the cell culture medium as shown in the Nyquist and Bode plots. Good fits are observed from the Nyquist and Bode plots, as well as the values of chi-square in Table 2. R_s corresponds to the solution resistance between the working electrode and reference electrode. The constant phase element, CPE_1, represents the capacitance of the oxidized surface layer or corrosion products and R_1 indicates the corresponding resistance against the mass transportation. CPE_2 is the double layer capacitance at the electrolyte/substrate surface and R_2 represents the relevant charge transfer resistance. According to the two electrical equivalent circuits, the fitted values are obtained from the Nyquist plots of the WE43 samples before and after ion implantation as listed in Table 2. Theoretically, the R_s values should be the same for alloys with different compositions in the same solution. The R_s values obtained from the untreated and Nd-implanted WE43 are 17.97 Ω cm^2 and 14.82 Ω cm^2, respectively, which are not exactly the same but close. Hong et al. [48] and Moradi et al. [49] have also observed a small difference in R_s from the materials in the same solution. The relatively small difference in the solution resistance for different materials may be caused by experimental errors. Compared to the untreated substrate in SBF, the Nd-implanted sample exhibits an approximately 550-fold and 50-fold increase in R_1 and R_2 and an about 105-fold and 29-fold decrease in CPE_1 and CPE_2, respectively. R_1 and R_2 are two essential parameters to evaluate the corrosion resistance and good anti-corrosion property is achieved by large R_1 and R_2 usually corresponding to small CPE_1 and CPE_2. Generally, a $Mg(OH)_2$ layer is formed during initial immersion in the corrosive solution. The smaller R_1 and R_2 of the untreated WE43 are related to the $Mg(OH)_2$ layer with less protective ability, thus giving rise to easy

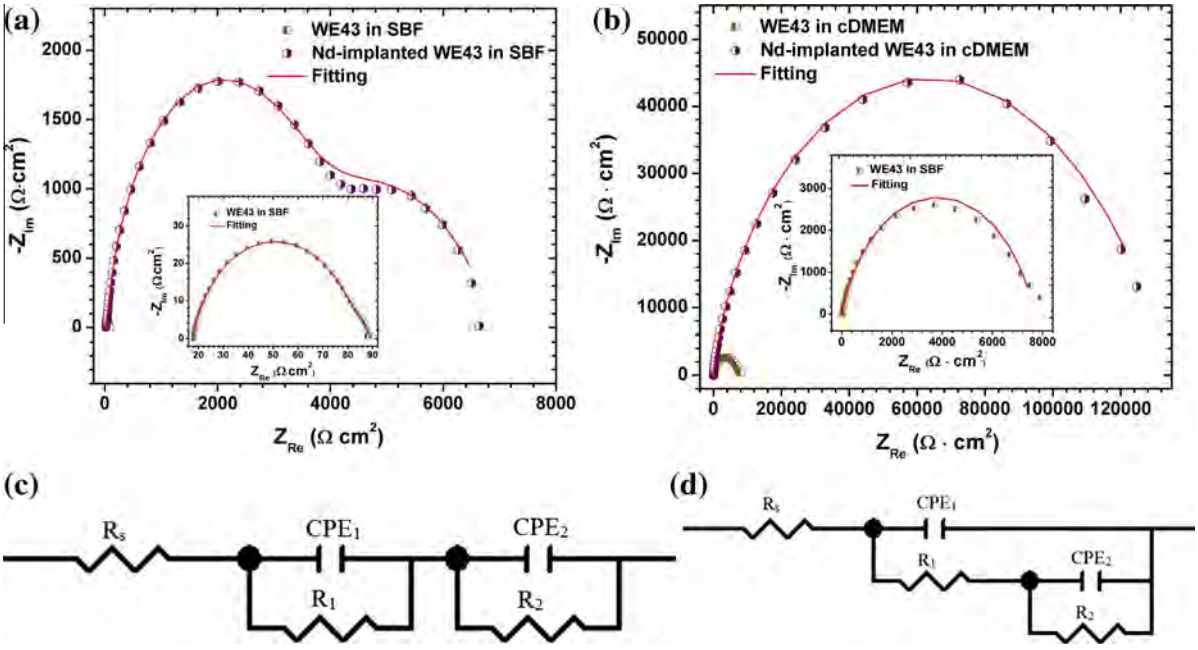

Fig. 8. Nyquist plots of the untreated and Nd-implanted WE43 in (a) SBF and (b) cDMEM and equivalent circuits of the untreated and Nd-implanted WE43 in (c) SBF and (d) cDMEM.

Table 2
Fitted EIS results of WE43 and Nd-implanted WE43 in SBF and cDMEM based on the corresponding equivalent circuit models.

	SBF		cDMEM	
	WE43	Nd-implanted WE43	WE43	Nd-implanted WE43
R_s (Ω cm^2)	17.97	14.82	16.93	16.69
CPE_1 (Ω^{-2} cm^{-2} S^{-n})	7.294×10^{-3}	6.954×10^{-5}	1.740×10^{-5}	1.667×10^{-6}
n_1	0.80	0.59	0.79	0.64
R_1 (Ω cm^2)	6.59	3626	135.3	18.16
CPE_2 (Ω^{-2} cm^{-2} S^{-n})	3.45×10^{-5}	1.17×10^{-6}	8.06×10^{-7}	3.07×10^{-7}
n_2	0.85	0.94	1	1
R_2 (Ω cm^2)	64.42	3253	7.511×10^3	1.351×10^5
χ^2	3.75×10^{-5}	7.06×10^{-4}	7.76×10^{-4}	2.58×10^{-4}

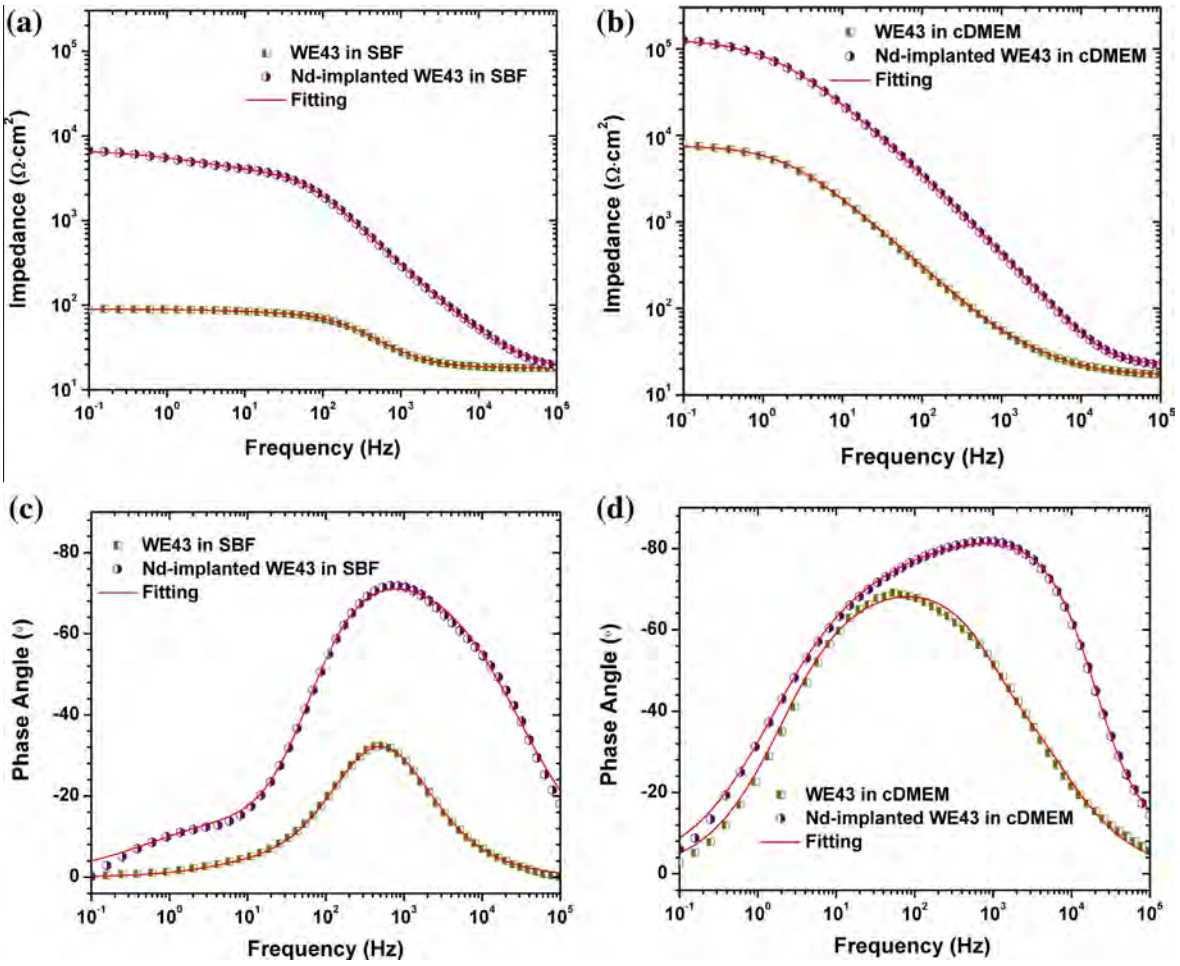

Fig. 9. (a and b) Bode impedance and (c and d) Bode phase angle plots of the untreated and Nd-implanted WE43 in SBF and cDMEM.

attack by the corrosive chloride ions and other species diffusing through the porous structure. The $Mg(OH)_2$ layer tends to be dissolved in the SBF with abundant chloride ions, thus exposing the magnesium substrate underneath for more corrosion. This porous layer also has a poor ability to resist mass transportation, thereby making it easier for chloride ions to penetrate the magnesium substrate. Thus, the native corrosion layer formed on the untreated WE43 tends to rupture and cannot protect the substrate. On the other hand, the significantly larger R_1 and R_2 of the Nd-implanted WE43 are attributed to the protective gradient layer containing Nd_2O_3 and MgO formed by Nd ion implantation. The stable and protective Nd_2O_3 is mainly responsible for the anti-corrosion properties while the inner MgO layer reinforces the protection of the substrate [50–52]. In the cell culture medium, the two capacitive loops interact with each other, which can be seen from the Nyquist and Bode plots. It is difficult to separate the components of the electrical equivalent circuits. Therefore, a much larger R_2 value but a smaller R_1 value is observed for the Nd-implanted WE43. In this condition, the anticorrosion properties of materials are usually evaluated by the sum of the R_1 and R_2 values [53]. Although the R_1 value of the Nd-implanted WE43 is smaller than that of the untreated WE43 in the cell culture medium, the R_2 value is several orders of magnitude larger than the R_1 value and the R_2 value of the Nd-implanted WE43 is approximately 18 times as much as that of the untreated WE43. Compared to the untreated WE43 ($7.6463 \times 10^3\ \Omega\ cm^2$), the total resistance of the Nd-implanted WE43 increases to $1.3512 \times 10^5\ \Omega\ cm^2$, which indicates the corrosion resistance of the Nd-implanted WE43 is greatly higher than

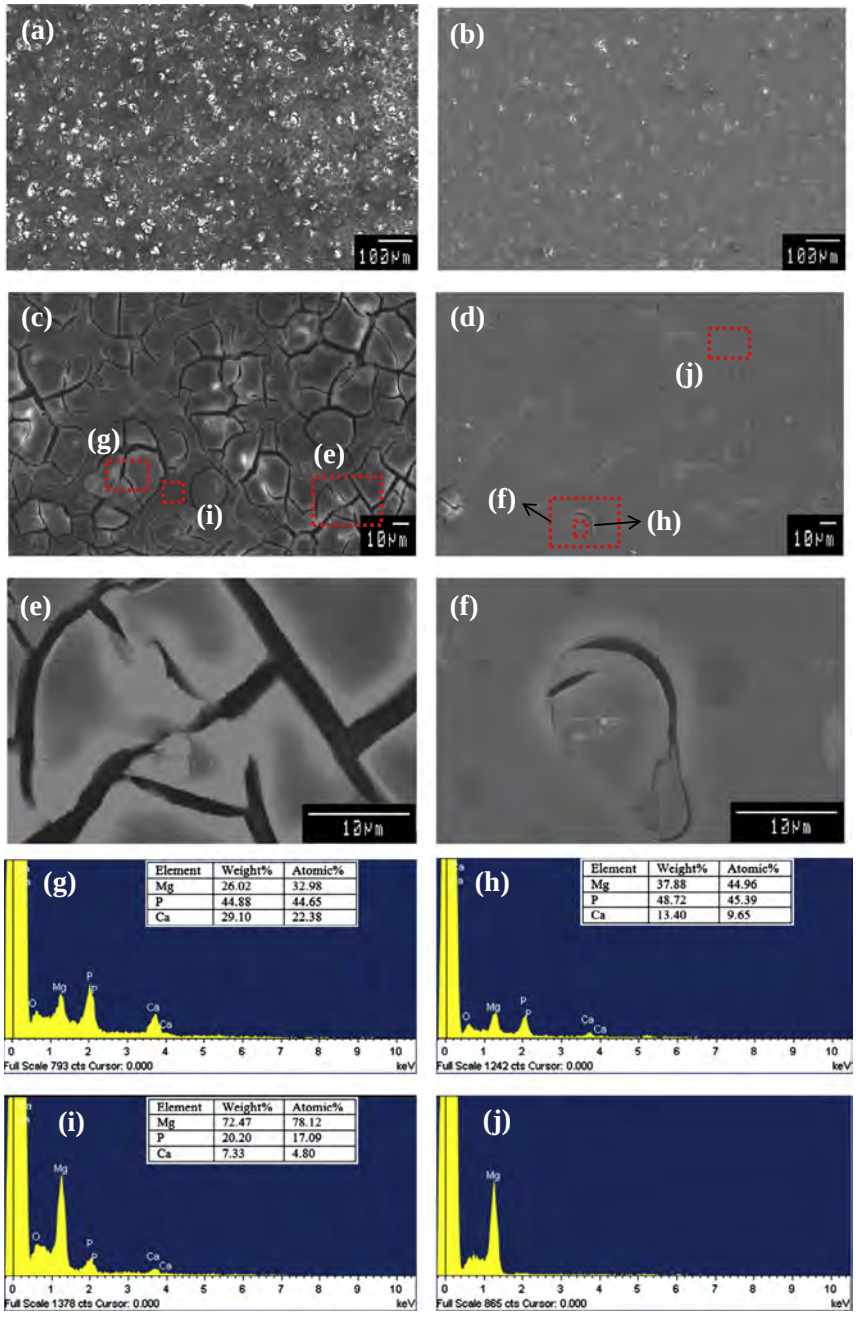

Fig. 10. Surface morphology at different magnifications and corresponding EDS spectra and quantitative analysis (Mg, Ca, and P) of (a, c, e, g, i) untreated and (b, d, f, h, j) Nd-implanted samples after immersed in SBF for 2 h.

that of the untreated WE43 in the cell culture medium. Compared to the untreated WE43, the Nd-implanted WE43 also shows a smaller CPE_1 in the cell culture medium. Generally, R_1 is inversely proportional to CPE_1. The nondistinct separation of the two interacting semicircles may also result in the deviation of the relationship between R_1 and CPE_1. It is not ideal in the actual simulation and has also observed by other researchers [54–56]. Thus, a small deviation in the R_1 and CPE_1 values should be acceptable. The results suggest that Nd ion implantation significantly enhances the corrosion resistance of the WE43 magnesium alloy in SBF and cell culture medium, although the improvement in the latter is not as substantial similar to the polarization curves.

Fig. 9 depicts the Bode impedance and phase angle plots of the untreated and Nd-implanted WE43 in SBF and cell culture medium. The Bode plots characterize the anticorrosion performance from different aspects and more direct information about the corrosion resistance can be obtained. Zahrani and Alfantazi [57], Cvijovic-Alagic et al. [58], and Osorio et al. [59] also discussed both the Nyquist and Bode plots in their papers. Compared to the untreated substrate, the Nd-implanted sample shows larger impedance and phase angle over the entire frequency range. The impedance of the Nd-implanted WE43 at the low frequency of 100 mHz shows a 86-fold increase in SBF and 11-fold increase in the cell culture medium. The maximum phase angle of the Nd-implanted WE43 increases from 32.1° ± 1.4 of the untreated WE43 to 73.0° ± 1.0 in SBF and from 67.8° ± 4.2 of the untreated WE43 to 81.7° ± 0.4 in the cell culture medium, respectively. According to the literature [60,61], the impedance at low frequency such as 100 mHz is an appropriate parameter to evaluate the protective properties and higher impedance at low frequency corresponds to better

protective performance because the impedance at the low frequency corresponds to the resistance against mass transportation of the dissolved ions through the oxidized/product layer. The remarkable increase of the impedance in the low frequency region of the Nd-implanted WE43 implies greatly improved corrosion resistance in the corrosive media. The larger phase angle corresponds to the more capacitive response which indicates that penetration of the corrosive solution through the oxidized/product layer to the substrate becomes weak and the current flowing through the defects in the oxidized/product layer becomes less significant [62]. The maximum phase angle peak at the higher frequency is mainly due to the formation of the surface film on the electrode surface [63] and a larger the maximum phase angle corresponds to better corrosion resistance. Hence, the corrosion resistance is enhanced in both SBF and cell culture medium. In addition, the improvement in both the maximum phase angle and impedance at low frequencies is more obvious in SBF than the cell culture medium, implying that Nd ion implantation can enhance the corrosion resistance in the both corrosive media, albeit more effective in SBF. The Bode impedance and phase angle results are consistent with those obtained by polarization and Nyquist studies.

Figs. 10–12 show the surface morphology at different magnification and corresponding EDS data of the untreated and Nd-implanted WE43 samples after immersion in SBF for 2, 12, and 36 h. According to the surface morphology images, severe corrosion is observed from the untreated WE43 surface after immersion in SBF but there is less local corrosion on the Nd-implanted surface even after immersion in SBF for 36 h. The corroded regions show

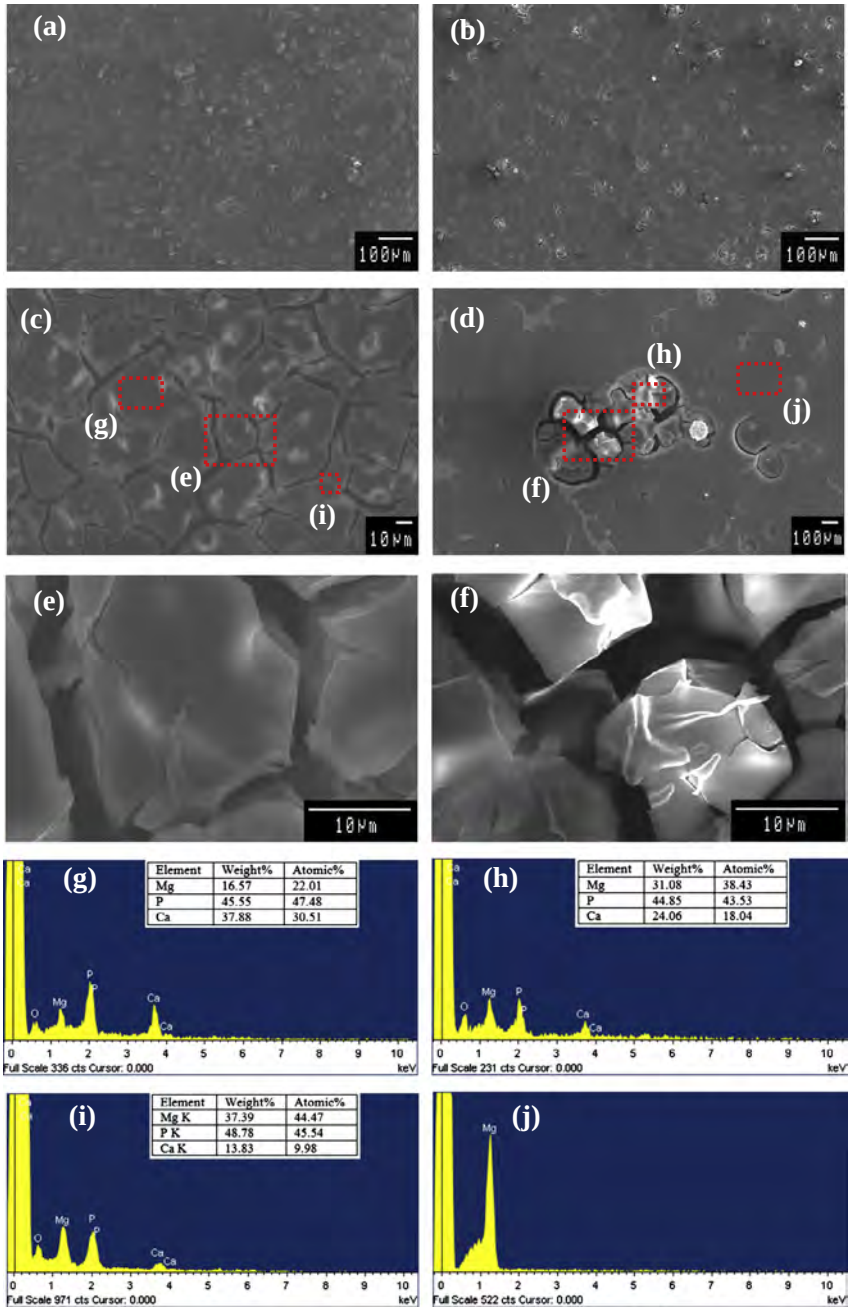

Fig. 11. Surface morphology at different magnifications and corresponding EDS spectra and quantitative analysis (Mg, Ca, and P) of (a, c, e, g, i) untreated and (b, d, f, h, j) Nd-implanted samples after immersed in SBF for 12 h.

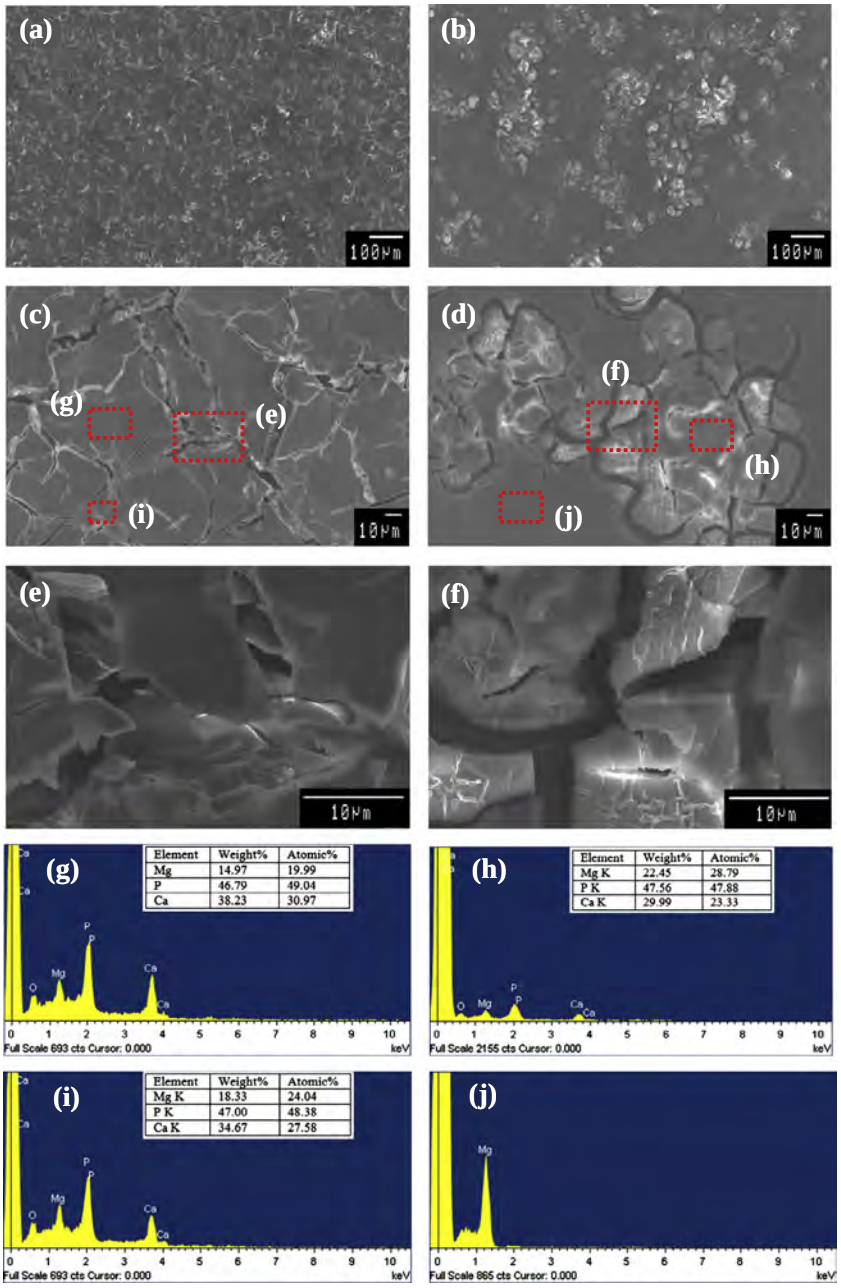

Fig. 12. Surface morphology at different magnifications and corresponding EDS spectra and quantitative analysis (Mg, Ca, and P) of (a, c, e, g, i) untreated and (b, d, f, h, j) Nd-implanted samples after immersed in SBF for 36 h.

some cracks which tend to become channels for penetration of the corrosive solution leading to further corrosion of the magnesium substrate. Only slight corrosion is observed from the Nd-implanted WE43 sample surface after immersion for 2 h, although some cracks appear after 12 and 36 h. However, the corroded area is still much less than that on the untreated sample. According to EDS, the corrosion products on the untreated and Nd-implanted WE43 samples immersed in SBF consist of Mg, O, Ca, and P stemming from MgO, $Mg(OH)_2$, phosphate, and carbonate. The same elements but different ratios are observed after immersion for different time. The EDS data are collected from the severely corroded regions (Figs. 10(g) and (i), 11(g) and (i), and 12(g) and (i)) and slightly or un-corroded regions (Figs. 10(h) and (j), 11(h) and (j), and 12(h) and (j)). The tabulated analysis shows only the relative amounts of Mg, Ca, and P, but O is not determined quantitatively. The quantitative analysis of all the elements is preferred and can provide more persuasive information. Generally, EDS is semi-quantitative. If light elements with atomic numbers less than 11 such as oxygen are included, the elemental contents deviate from the actual values. For instance, Jamesh [64] determined the elemental contents by EDS by including only the relatively heavy elements such as Mg, Ca, and P. Determination of the relative concentrations of heavy elements imparts useful information about the corrosion products and here, we show the concentration of these important elements excluding oxygen. Compared to the untreated WE43 sample, the Nd-implanted WE43 samples have smaller concentrations of Ca and P but larger amount of Mg and a similar trend is observed from the seriously corroded areas as well. Even after immersion for 36 h, there are still some regions showing Mg on the Nd-implanted sample, indicating the absence of corrosion.

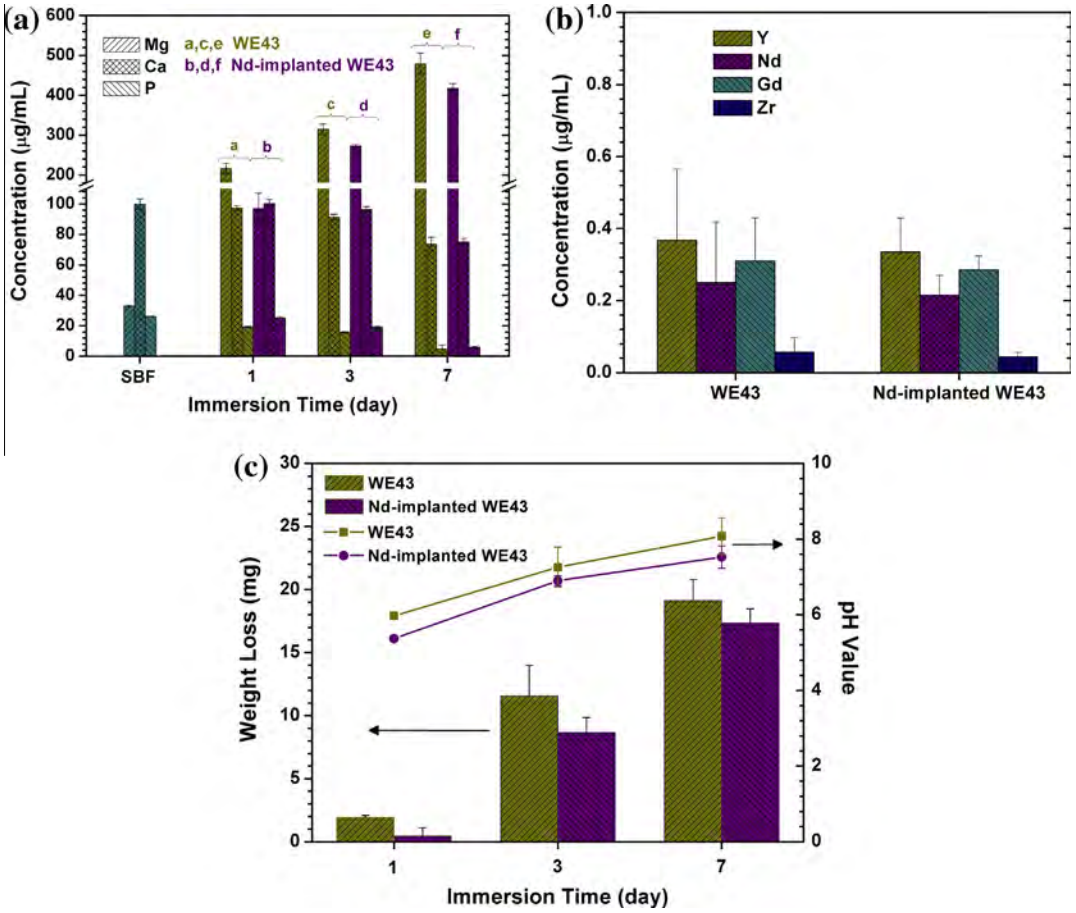

Fig. 13. Concentrations of (a) Mg, Ca, and P at 1, 3, and 7 days and (b) alloy elements at 7 days for the untreated and Nd-implanted WE43 samples in SBF. (c) Weight loss of the untreated and Nd-implanted WE43 samples and pH values of the extracted SBF of the untreated and Nd-implanted WE43 samples at 1, 3, and 7 days.

These results suggest that corrosion of the untreated and Nd-implanted WE43 surface continues with immersion time, but the corrosion propagation is much slower on the Nd-implanted WE43 sample.

Fig. 13(a) shows the concentrations of Mg, Ca, and P released from the untreated and Nd-implanted WE43 samples determined by ICP-OES. The Mg ion concentration increases gradually with immersion time as expected. After 1 day, the Mg concentration released from the implanted sample is only 97.0 ppm, which is much smaller than 216.3 ppm released from the untreated WE43 sample. Even after 3 and 7 days, the Nd-implanted WE43 sample releases much less Mg than the untreated WE43 sample. In addition, compared to fresh SBF, the Ca and P concentrations of both the untreated and Nd-implanted WE43 exhibit no big change in the beginning and then decrease due to the insoluble Ca and P corrosion products. Small concentrations of Ca and P are observed from the untreated WE43 samples, which is in accordance with the larger Ca and P contents in the corrosion products of the untreated WE43 sample as shown by EDS. The alloying element concentrations leached from the untreated and Nd-implanted WE43 are also determined to be less than 0.4 μg/mL, as shown in Fig. 13(b), while the concentrations measured from the extracted SBF of the Nd-implanted WE43 samples are smaller than those determined from the extracted SBF of the untreated WE43. Fig. 13(c) presents the corresponding pH values measured from the extracted SBF of the untreated and Nd-implanted WE43 samples. A gradual increase in the pH over time is observed from the untreated and Nd-implanted WE43 samples. The pH increases from 7.99 to 9.04 for the untreated WE43 and varies between 7.68 and 8.76 for the Nd-implanted WE43. As shown in Fig. 13(c), the weight losses measured from the Nd-implanted WE43 samples are obviously smaller than those measured from the untreated WE43 samples at each time interval. All in all, the immersion test furnishes experimental evidence that the degradation rate of the WE43 magnesium alloy is mitigated by Nd ion implantation.

To fathom the corrosion process and reason for the improved corrosion resistance of the WE43 magnesium, the mechanism proposed by Song [65] is adopted here. After immersion in the solution, the magnesium matrix surrounding the second phase dissolves (Eq. (1)) because the second phase is nobler and less reactive than the magnesium matrix being the anodic electrode [66]. Simultaneously, hydrogen is produced due to the cathodic reaction (Eq. (2)), which results in a local alkaline condition. A magnesium hydroxide $Mg(OH)_2$ layer with a porous structure is formed (Eq. (3)) in the corrosion regions due to the favorable alkaline environment as follows:

$$Mg\ (s) \rightarrow Mg^{2+}\ (aq) + 2e^{-} \quad \text{(anodic reaction)} \tag{1}$$

$$2H_2O\ (aq) + 2e^{-} \rightarrow H_2\ (g) + 2OH^{-}\ (aq) \quad \text{(cathodic reaction)} \tag{2}$$

$$Mg^{2+}\ (aq) + 2OH^{-}\ (aq) \rightarrow Mg(OH)_2\ (s) \quad \text{(product formation)} \tag{3}$$

$$Mg\ (s) + 2H_2O\ (aq) \rightarrow Mg(OH)_2\ (s) + H_2\ (g) \quad \text{(overall reaction)} \tag{4}$$

The $Mg(OH)_2$ corrosion layer formed on the magnesium alloys is stable only in an alkaline solution with a pH of over 11.5 [67]. Therefore, the insoluble $Mg(OH)_2$ is normally transformed into insoluble $MgCl_2$ in a solution with corrosive chloride ions. The process continues into the substrate until the corrosion medium is exhausted. Accompanying the corrosion process, hydroxyapatite is formed because the previously formed $Mg(OH)_2$ provides favorable sites for hydroxyapatites nucleation and its continuous growth is maintained by consuming Ca and P species in the surrounding solution. The magnesium dissolution process increases the Mg, as well as alloying element concentrations, but decreases the Ca and P concentration in the corrosive solution, resulting in increasing pH and formation of the corrosion products containing Mg, O, Ca, and P. In comparison with the untreated WE43 magnesium alloy, the Nd-implanted WE43 is better protected by the implanted layer containing stable and protective Nd_2O_3 and partially-protective MgO. The oxide layer serves as a strong barrier against corrosion and greatly retards magnesium dissolution. Nevertheless, there are still a few regions on the Nd-implanted WE43 sample not covered well by the oxide. In these regions, the corrosive solution can still overcome the surface layer to reach the substrate, giving rise to local corrosion of the Nd-implanted WE43 surface. The area of the substrate exposed to the corrosive solution is restricted by the oxide layer and the implanted layer is able to effectively delay the corrosion process of the magnesium alloy [53]. Therefore, a smaller degradation rate is observed from the Nd-implanted WE43 and the ensuing environmental changes induced by the Nd-implanted WE43 are much less than those by the untreated WE43. The environmental changes can influence the biological properties of the magnesium alloys to be discussed in the next section.

3.3. In vitro studies

Fig. 14 displays the MC3T3-E1 cell morphology on the untreated and Nd-implanted WE43 samples after incubation for 5 h. It clearly shows that the number of MC3T3-E1 cells on the Nd-implanted sample is significantly larger than that on the untreated one, implying better initial cell adhesion after the surface treatment. In addition, the MC3T3-E1 cells on the Nd-implanted WE43 sample spread better and have better shape because the attached cells have more flattened membranes and filopodia corresponding to good cell attachment to the materials surface. Compared to the untreated WE43, the Nd-implanted sample exhibits better cell adhesion.

Fig. 15 shows the viability of the MC3T3-E1 pre-osteoblasts cultured in the WE43 and Nd-implanted WE43 extraction media with 100%, 70%, 50%, and 10% concentrations for 1 and 3 days. The cell viability is expressed as a percentage of the viability of cells cultured on the control. The viability of the MC3T3-E1 pre-osteoblasts cultured in the extraction medium of the Nd-implanted WE43 sample is close to that of the control at each concentration after incubation for 1 day and similar values are observed after 3 days. However, the untreated WE43 extraction medium, especially at high concentrations, shows significantly reduced cell viability. The MC3T3-E1 cells after incubation with the untreated WE43 extraction medium for 3 days display obviously decreased cell viability. This indicates that the untreated WE43 has high cytotoxicity to the MC3T3-E1 pre-osteoblasts. In comparison with the untreated WE43, the Nd-implanted WE43 shows better biocompatibility.

Besides the good corrosion resistance, good biological properties are required for implantable biomaterials. The Nd-implanted WE43 sample exhibits good cell adhesion and viability. It is possibly because the formation of a relatively smooth, hydrophobic, anti-corrosion, and biocompatible surface layer containing Nd_2O_3 and MgO provides a more stable and favorable environment for cell attachment and cell growth. Other surface characteristics, such as composition, surface roughness, and surface energy, can also influence the cell response, such as adhesion, spreading, and proliferation. Here, the surface properties affect direct cell adhesion due to the direct contact between the cells and materials surface, while there is less influence on indirect cell viability. Cells that spread better tend to proliferate better, and thus, good cell attachment is important to promoting proliferation. A relatively smooth surface has been shown to contribute to better cell adhesion [68–70]. The Nd-implanted WE43 sample is not as rough as the untreated one, and therefore, the MC3T3-E1 pre-osteoblasts cultured on the untreated WE43 sample spread less and also have a more abnormal shape. In contrast, cells cultured on the

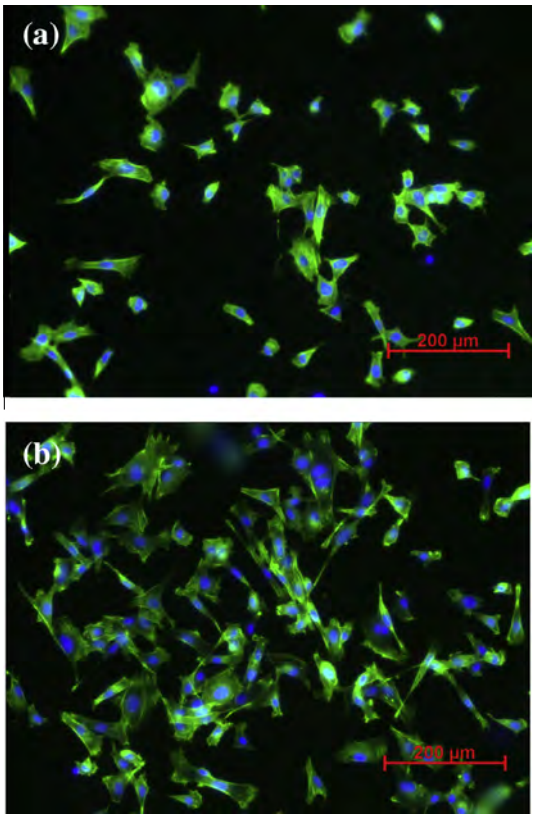

Fig. 14. Fluorescent images of MC3T3-E1 pre-oteoblasts after 5 h incubation on the (a) untreated and (b) Nd-implanted WE43 samples.

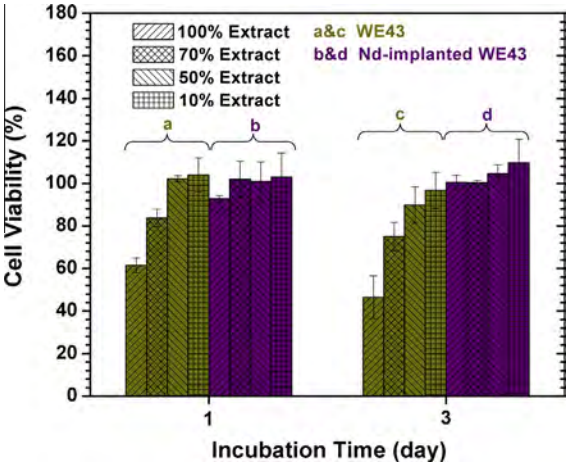

Fig. 15. *In vitro* cell viability of MC3T3-E1 pre-oteoblasts cultured in the extraction medium of the untreated and Nd-implanted WE43 for 1 and 3 days.

Nd-implanted WE43 sample are large in number, spread well, and have a normal shape. As another important factor affecting the cellular behavior, the surface energy of the implantable materials can regulate cell adhesion, spreading, and proliferation. One general observation is that hydrophobic surfaces are beneficial to cell adhesion and proliferation [71,72]. Hence, the lower surface energy on the Nd-implanted WE43 results in better cell attachment. Some researchers have studied the relationship between the contact angle and cellular behavior. The surface interactions are very complex and surface free energy is not correlated to wettability only. Some studies show that a 60–70° contact angle is ideal for cell attachment and spreading and 65° is commonly regarded as the magical value for implantable materials [73,74]. The contact angle of the Nd-implanted WE43 increases from 35.8° to 71.2°, thus boding well for osteoblasts.

The enhanced biological properties of the magnesium alloys are generally related to the improved corrosion resistance [16]. Rapid degradation of magnesium results in excessive formation of corrosion products, such as released metal ions, alkaline environment, and hydrogen bubbles. Cells are very sensitive to environmental fluctuations. Owing to the improved corrosion resistance, the Nd-implanted WE43 sample is able to provide an environment with a pH closer to the normal physiological environment, thus benefitting cell adhesion and growth. The amounts of released Mg and alloying elements from the Nd-implanted WE43 samples are also smaller thus giving rise to the better cell attachment and cell viability [75]. Theoretically, the improved corrosion resistance leads to less hydrogen evolution, thereby providing a stable surface with good biocompatibility. Hydrogen evolution may negatively influence direct cell adhesion because better cell attachment and cell viability are achieved when the cells are cultured in a friendly environment with less adverse stimulation.

4. Conclusion

Rapid degradation of rare-earth magnesium alloys is the major limitation hampering wider application to cardiovascular stents and orthopedic implants. To improve the corrosion resistance of the WE43 magnesium alloy, low-fluence Nd self-ion implantation, which does not involve elements foreign to the alloy, is performed. The XPS, SEM, AFM, and water contact angle results show that a relatively smooth and hydrophobic surface layer composed of mainly Nd_2O_3 and MgO is produced. The Nd-implanted sample exhibits a significantly smaller corrosion current density and higher impedance in both SBF and cell culture medium. Smaller weight loss, smaller pH variation, less leaching of magnesium and alloying elements, and much less severe corrosion are observed from the Nd-implanted WE43 magnesium alloy. The remarkable enhancement in the corrosion resistance is mainly attributed to the stable and protective Nd_2O_3 outer layer, as well as partially protective MgO inner layer. Cells attach and spread well on the Nd-implanted WE43 and cells incubated with the extracted medium of the Nd-implanted WE43 for 3 days show similar viability obtained from the complete cell culture medium, indicating that the Nd-implanted WE43 magnesium alloy has good biocompatibility *in vitro*. The improvement in the *in vitro* biological response stems from the improved corrosion resistance and relatively hydrophobic and smooth surface. Our results suggest that Nd self-ion implantation is a promising method to improve both the corrosion resistance and *in vitro* biocompatibility of the rare-earth WE43 magnesium alloy.

Acknowledgments

This work is financially supported by City University of Hong Kong Research Grants Council (RGC) General Research Funds (GRF) CityU 112212, and Hong Kong Strategic Research Grant (SRG) No. 7004188.

References

[1] R. Waksman, R. Pakala, P.K. Kuchulakanti, R. Baffour, D. Hellinga, R. Seabron, F.O. Tio, E. Wittchow, S. Hartwig, C. Harder, R. Rohde, B. Heublein, A. Andreae, K.H. Waldmann, A. Haverich, Safety and efficacy of bioabsorbable magnesium alloy stents in porcine coronary arteries, Catheter. Cardiovasc. Interv. 68 (2006) 607–617.
[2] R. Erbel, C. Di Mario, J. Bartunek, J. Bonnier, B. de Bruyne, F.R. Eberli, P. Erne, M. Haude, B. Heublein, M. Horrigan, C. Ilsley, D. Bose, J. Koolen, T.F. Luscher, N. Weissman, R. Waksman, P.A. Investigators, Temporary scaffolding of coronary arteries with bioabsorbable magnesium stents: a prospective, non-randomised multicentre trial, Lancet 369 (2007) 1869–1875.
[3] P. Zartner, R. Cesnjevar, H. Singer, M. Weyand, First successful implantation of a biodegradable metal stent into the left pulmonary artery of a preterm baby, Catheter. Cardiovasc. Interv. 66 (2005) 590–594.
[4] F. Witte, V. Kaese, H. Haferkamp, E. Switzer, A. Meyer-Lindenberg, C.J. Wirth, H. Windhagen, In vivo corrosion of four magnesium alloys and the associated bone response, Biomaterials 26 (2005) 3557–3563.
[5] F. Witte, J. Fischer, J. Nellesen, H.A. Crostack, V. Kaese, A. Pisch, F. Beckmann, H. Windhagen, In vitro and in vivo corrosion measurements of magnesium alloys, Biomaterials 27 (2006) 1013–1018.
[6] G. Levy, E. Aghion, Effect of diffusion coating of Nd on the corrosion resistance of biodegradable Mg implants in simulated physiological electrolyte, Acta Biomater. 9 (2013) 8624–8630.
[7] H. Hermawan, D. Dube, D. Mantovani, Developments in metallic biodegradable stents, Acta Biomater. 6 (2010) 1693–1697.
[8] M.P. Staiger, A.M. Pietak, J. Huadmai, G. Dias, Magnesium and its alloys as orthopedic biomaterials: a review, Biomaterials 27 (2006) 1728–1734.
[9] Y. Ding, C. Wen, P. Hodgson, Y. Li, Effects of alloying elements on the corrosion behavior and biocompatibility of biodegradable magnesium alloys: a review, J. Mater. Chem. B 2 (2014) 1912–1933.
[10] X. Gu, Y. Zheng, Y. Cheng, S. Zhong, T. Xi, In vitro corrosion and biocompatibility of binary magnesium alloys, Biomaterials 30 (2009) 484–498.
[11] C.D. Mario, H. Griffiths, O. Goktekin, N. Peeters, J. Verbist, M. Bosiers, K. Deloose, B. Heublein, R. Rohde, V. Kasese, C. Ilsley, R. Erbel, Drug-eluting bioabsorbable magnesium stent, J. Interv. Cardiol. 17 (2004) 391–395.
[12] L.L. Rokhlin, Magnesium Alloys Containing Rare Earth Metals: Structure and Properties, Taylor und Francis, London, 2003.
[13] T. Zhang, G. Meng, Y. Shao, Z. Cui, F. Wang, Corrosion of hot extrusion AZ91 magnesium alloy. Part II: effect of rare earth element neodymium (Nd) on the corrosion behavior of extruded alloy, Corros. Sci. 53 (2011) 2934–2942.
[14] F. Witte, N. Hort, C. Vogt, S. Cohen, K.U. Kainer, R. Willumeit, F. Feyerabend, Degradable biomaterials based on magnesium corrosion, Curr. Opin. Solid State Mater. Sci. 12 (2008) 63–72.
[15] N. Liu, J. Wang, L. Wang, Y. Wu, L. Wang, Electrochemical corrosion behavior of Mg–5Al–0.4Mn–xNd in NaCl solution, Corros. Sci. 51 (2009) 1328–1333.
[16] Y. Zhao, M.I. Jamesh, W.K. Li, G. Wu, C. Wang, Y. Zheng, K.W.K. Yeung, P.K. Chu, Enhanced antimicrobial properties, cytocompatibility, and corrosion resistance of plasma-modified biodegradable magnesium alloys, Acta Biomater. 10 (2014) 544–556.
[17] F. Feyerabend, J. Fischer, J. Holtz, F. Witte, R. Willumeit, H. Druecker, C. Vogt, N. Hort, Evaluation of short-term effects of rare earth and other elements used in magnesium alloys on primary cells and cell lines, Acta Biomater. 6 (2010) 1834–1842.
[18] G. Song, Control of biodegradation of biocompatable magnesium alloys, Corros. Sci. 49 (2007) 1696–1701.
[19] H. Hornberger, S. Virtanen, A.R. Boccaccini, Biomedical coatings on magnesium alloys – a review, Acta Biomater. 8 (2012) 2442–2455.
[20] S. Shadanbaz, G.J. Dias, Calcium phosphate coatings on magnesium alloys for biomedical applications: a review, Acta Biomater. 8 (2012) 20–30.
[21] M. Moravej, D. Mantovani, Biodegradable metals for cardiovascular stent application: interests and new opportunities, Int. J. Mol. Sci. 12 (2011) 4250–4270.
[22] G. Jin, Y. Yang, X. Cui, E. Liu, Z. Wang, Q. Li, Chrome-free neodymium-based protective coatings for magnesium alloys, Mater. Lett. 65 (2011) 1145–1147.
[23] M.I. Jamesh, G. Wu, Y. Zhao, D.R. McKenzie, M.M.M. Bilek, P.K. Chu, Effects of zirconium and oxygen plasma ion implantation on the corrosion behavior of ZK60 Mg alloy in simulated body fluids, Corros. Sci. 82 (2014) 7–26.
[24] G. Wu, R. Xu, K. Feng, S. Wu, Z. Wu, G. Sun, G. Zheng, G. Li, P.K. Chu, Retardation of surface corrosion of biodegradable magnesium-based materials by aluminum ion implantation, Appl. Surf. Sci. 258 (2012) 7651–7657.
[25] J.M. Seitz, R. Eifler, J. Stahl, M. Kietzmann, F.W. Bach, Characterization of MgNd2 alloy for potential applications in bioresorbable implantable devices, Acta Biomater. 8 (2012) 3852–3864.
[26] J. Zhang, J. Wang, X. Qiu, D. Zhang, Z. Tian, X. Niu, D. Tang, J. Meng, Effect of Nd on the microstructure, mechanical properties and corrosion behavior of die-cast Mg–4Al-based alloy, J. Alloys Compd. 464 (2008) 556–564.
[27] T. Takenaka, T. Ono, Y. Narazaki, Y. Naka, M. Kawakami, Improvement of corrosion resistance of magnesium metal by rare earth elements, Electrochim. Acta 53 (2007) 117–121.
[28] R. Arrabal, E. Matykina, A. Pardo, M.C. Merino, K. Paucar, M. Mohedano, P. Casajus, Corrosion behaviour of AZ91D and AM50 magnesium alloys with Nd and Gd additions in humid environments, Corros. Sci. 55 (2012) 351–362.

[29] Y.L. Song, Y.H. Liu, S.R. Yu, X.Y. Zhu, S.H. Wang, Effect of neodymium on microstructure and corrosion resistance of AZ91 magnesium alloy, J. Mater. Sci. 42 (2007) 4435–4440.
[30] Q. Wang, W. Jin, G. Wu, Y. Zhao, X. Jin, X. Hu, J. Zhou, G. Tang, P.K. Chu, Rare-earth-incorporated polymeric vector for enhanced gene delivery, Biomaterials 35 (2014) 479–488.
[31] T. Kokubo, H. Takadama, How useful is SBF in predicting in vivo bone bioactivity?, Biomaterials 27 (2006) 2907–2915
[32] M. Liu, S. Zanna, H. Ardelean, I. Frateur, P. Schmutz, G. Song, A. Atrens, P. Marcus, A first quantitative XPS study of the surface films formed, by exposure to water, on Mg and on the Mg–Al intermetallics: Al_3Mg_2 and $Mg_{17}Al_{12}$, Corros. Sci. 51 (2009) 1115–1127.
[33] Y. Zhao, G. Wu, Q. Lu, J. Wu, R. Xu, K.W.K. Yeung, P.K. Chu, Improved surface corrosion resistance of WE43 magnesium alloy by dual titanium and oxygen ion implantation, Thin Solid Films 529 (2013) 407–411.
[34] J.F. Moulder, W.F. Stickle, P.E. Sobol, K.D. Bomben, Handbook of X-ray Photoelectron Spectroscopy, Perkin–Elmer Corporation, Minnesota, 1992.
[35] M. Jamesh, G. Wu, Y. Zhao, P.K. Chu, Effects of silicon plasma ion implantation on electrochemical corrosion behavior of biodegradable Mg–Y–RE alloy, Corros. Sci. 69 (2013) 158–163.
[36] R. Walter, M.B. Kannan, Influence of surface roughness on the corrosion behaviour of magnesium alloy, Mater. Des. 32 (2011) 2350–2354.
[37] B. Yoo, K.R. Shin, D.Y. Hwang, D.H. Lee, D.H. Shin, Effect of surface roughness on leakage current and corrosion resistance of oxide layer on AZ91 Mg alloy prepared by plasma electrolytic oxidation, Appl. Surf. Sci. 256 (2010) 6667–6672.
[38] W. Li, D.Y. Li, Influence of surface morphology on corrosion and electronic behavior, Acta Mater. 54 (2006) 445–452.
[39] J.F. Dyet, W.G. Watts, D.F. Ettles, A.A. Nicholson, Mechanical properties of metallic stents: how do these properties influence the choice of stent for specific lesions?, Cardiovasc Intervent. Radiol. 23 (2000) 47–54.
[40] P. Zhang, S.X. Li, Z.F. Zhang, General relationship between strength and hardness, Mater. Sci. Eng. A 529 (2011) 62–73.
[41] John J. Oilman, Dislocation Motions and the Yield Strength of Solids, American Society for Testing and Materials, USA, 1961. pp. 69–81.
[42] H. Wang, M. Xu, W. Zhang, D.T.K. Kwok, J. Jiang, Z. Wu, P.K. Chu, Mechanical and biological characteristics of diamond-like carbon coated poly aryl-ether-ether-ketone, Biomaterials 31 (2010) 8181–8187.
[43] L. Tan, Q. Wang, X. Lin, P. Wan, G. Zhang, Q. Zhang, K. Yang, Loss of mechanical properties in vivo and bone-implant interface strength of AZ31B magnesium alloy screws with Si-containing coating, Acta Biomater. 10 (2014) 2333–2340.
[44] E. McCafferty, Validation of corrosion rates measured by the Tafel extrapolation method, Corros. Sci. 47 (2005) 3202–3215.
[45] G.L. Song, Recent progress in corrosion and protection of magnesium alloys, Adv. Eng. Mater. 7 (2005) 563–586.
[46] C.L. Liu, Y.J. Wang, R.C. Zeng, X.M. Zhang, W.J. Huang, P.K. Chu, In vitro corrosion degradation behaviour of Mg–Ca alloy in the presence of albumin, Corros. Sci. 52 (2010) 3341–3347.
[47] S.J. Garcia, T.A. Markley, J.M.C. Mol, A.E. Hughes, Unravelling the corrosion inhibition mechanisms of bi-functional inhibitors by EIS and SEM-EDS, Corros. Sci. 69 (2013) 346–358.
[48] T. He, Y. Wang, Y. Zhang, Q. Iv, T. Xu, T. Liu, Super-hydrophobic surface treatment as corrosion protection for aluminum in seawater, Corros. Sci. 51 (2009) 1757–1761.
[49] P. Ocon, A.B. Cristobal, P. Herrasti, E. Fatas, Corrosion performance of conducting polymer coatings applied on mild steel, Corros. Sci. 47 (2005) 649–662.
[50] T. Lei, C. Ouyang, W. Tang, L.F. Li, L.S. Zhou, Enhanced corrosion protection of MgO coatings on magnesium alloy deposited by an anodic electrodeposition process, Corros. Sci. 52 (2010) 3504–3508.
[51] Y.J. Zhang, C.W. Yan, F.H. Wang, W.F. Li, Electrochemical behavior of anodized Mg alloy AZ91D in chloride containing aqueous solution, Corros. Sci. 47 (2005) 2816–2831.
[52] M.J. Wang, C.F. Li, S.K. Yen, Electrolytic MgO/ZrO_2 duplex-layer coating on AZ91D magnesium alloy for corrosion resistance, Corros. Sci. 76 (2013) 142–153.
[53] G.L. Song, Z. Shi, Corrosion mechanism and evaluation of anodized magnesium alloys, Corros. Sci. 85 (2014) 126–140.
[54] W.R. Osorio, E.S. Freitas, J.E. Spinelli, A. Garcia, Electrochemical behavior of a lead-free Sn–Cu solder alloy in NaCl solution, Corros. Sci. 80 (2014) 71–81.
[55] G.A. El-Mahdy, A. Nishikata, T. Tsuru, AC impedance study on corrosion of 55%Al–Zn alloy-coated steel under thin electrolyte layers, Corros. Sci. 42 (2000) 1509–1521.
[56] M.S. Morad, Inhibition of iron corrosion in acid solutions by Cefatrexyl: behaviour near and at the corrosion potential, Corros. Sci. 50 (2008) 436–448.
[57] E.M. Zahrani, A.M. Alfantazi, High temperature corrosion and electrochemical behavior of INCONEL 625 weld overlay in $PbSO_4$–Pb_3O_4–$PbCl_2$–CdO–ZnO molten salt medium, Corros. Sci. 85 (2014) 60–76.
[58] I. Cvijovic-Alagic, Z. Cvijovic, J. Bajat, M. Rakin, Composition and processing effects on the electrochemical characteristics of biomedical titanium alloys, Corros. Sci. 83 (2014) 245–254.
[59] W.R. Osorio, L.C. Peixoto, P.R. Goulart, A. Garcia, Electrochemical corrosion parameters of as-cast Al–Fe alloys in a NaCl solution, Corros. Sci. 52 (2010) 2979–2993.
[60] J.H. Park, G.D. Lee, A. Nishikata, T. Tsuru, Anticorrosive behavior of hydroxyapatite as an environmentally friendly pigment, Corros. Sci. 44 (2002) 1087–1095.
[61] Y. Chen, X.H. Wang, J. Li, J.L. Lu, F.S. Wang, Long-term anticorrosion behaviour of polyaniline on mild steel, Corros. Sci. 49 (2007) 3052–3063.
[62] C. Liu, Q. Bi, A. Leyland, A. Matthews, An electrochemical impedance spectroscopy study of the corrosion behaviour of PVD coated steels in 0.5 N NaCl aqueous solution: Part II. EIS interpretation of corrosion behaviour, Corros. Sci. 45 (2003) 1257–1273.
[63] S.L. Wu, Z.D. Cui, G.X. Zhao, M.L. Yan, S.L. Zhu, X.J. Yang, EIS study of the surface film on the surface of carbon steel from supercritical carbon dioxide corrosion, Appl. Surf. Sci. 228 (2004) 17–25.
[64] M.I. Jamesh, G. Wu, Y. Zhao, W. Jin, D.R. McKenzie, M.M.M. Bilek, P.K. Chu, Effects of zirconium and nitrogen plasma immersion ion implantation on the electrochemical corrosion behavior of Mg–Y–RE alloy in simulated body fluid and cell culture medium, Corros. Sci. 86 (2014) 239–251.
[65] G.L. Song, A. Atrens, Understanding magnesium corrosion – a framework for improved alloy performance, Adv. Eng. Mater. 5 (2003) 837–858.
[66] G.L. Song, A. Atrens, M. Dargusch, Influence of microstructure on the corrosion of diecast AZ91D, Corros. Sci. 41 (1999) 249–273.
[67] M. Pourbaix, Atlas of Electrochemical Equilibria in Aqueous Solution, Pergamon Press, London, 1966.
[68] T.P. Kunzler, T. Drobek, M. Schuler, N.D. Spencer, Systematic study of osteoblast and fibroblast response to roughness by means of surface-morphology gradients, Biomaterials 28 (2007) 2175–2182.
[69] J.Y. Lim, A.D. Dreiss, Z. Zhou, J.C. Hansen, C.A. Siedlecki, R.W. Hengstebeck, J. Cheng, N. Winograd, H.J. Donahue, The regulation of integrin-mediated osteoblast focal adhesion and focal adhesion kinase expression by nanoscale topography, Biomaterials 28 (2007) 1787–1797.
[70] K. Anselme, P. Linez, M. Bigerelle, D. Le Maguer, A. Le Maguer, P. Hardouin, H.F. Hildebrand, A. Iost, J.M. Leroy, The relative influence of the topography and chemistry of TiAl6V4 surfaces on osteoblastic cell behaviour, Biomaterials 21 (2000) 1567–1577.
[71] S.B. Kennedy, N.R. Washburn, C.G. Simon, E.J. Amis, Combinatorial screen of the effect of surface energy on fibronectin-mediated osteoblast adhesion, spreading and proliferation, Biomaterials 27 (2006) 3817–3824.
[72] M. Padial-Molina, P. Galindo-Moreno, J. Emilio Fernandez-Barbero, F. O'Valle, A. Belen Jodar-Reyes, J. Luis Ortega-Vinuesa, P.J. Ramon-Torregrosa, Role of wettability and nanoroughness on interactions between osteoblast and modified silicon surfaces, Acta Biomater. 7 (2011) 771–778.
[73] T. Groth, G. Altankov, Studies on cell-biomaterial interaction role of tyrosine phosphorylation during fibroblast spreading on surfaces varying in wettability, Biomaterials 17 (1996) 1227–1234.
[74] M.M. Gentleman, E. Gentleman, The role of surface free energy in osteoblast-biomaterial interactions, Int. Mater. Rev. 59 (2014) 417–429.
[75] H.M. Wong, S. Wu, P.K. Chu, S.H. Cheng, K.D.K. Luk, K.M.C. Cheung, K.W.K. Yeung, Low-modulus Mg/PCL hybrid bone substitute for osteoporotic fracture fixation, Biomaterials 34 (2013) 7016–7032.